Available online at www.sciencedirect.com
ScienceDirect
ELSEVIER
Flow Measurement and Instrumentation 18 (2007) 27–36
Flow Measurement and Instrumentation
www.elsevier.com/locate/flowmeasinst

Galvanometer-based PIV for liquid flows

T. Schlicke, S.M. Cameron, S.E. Coleman*

Department of Civil and Environmental Engineering, The University of Auckland, Private Bag 92019, Auckland, New Zealand

Received 9 June 2006; received in revised form 15 October 2006; accepted 19 December 2006

Abstract

A cost-effective Particle Image Velocimetry (PIV) system has been developed that is capable of resolving flow fields at frequencies of up to 200 Hz (covering the typical scales of interest for hydraulic researchers), with recording durations of over 8 min. The system uses a high-speed camera to image flow fields illuminated by a scanning-beam lightsheet, where the lightsheet is generated by a galvanometer-driven mirror (computer controlled) together with a parabolic mirror. The system has several advantages over rotating-polygon type scanning systems, including: that the mirror is always positioned at the focal point of the parabola, and that the lightsheet generation is extremely versatile, with the lightsheet width (for a single parabolic mirror) and beam scan velocities easily and independently adjustable. Additionally, the beam scan velocity, which is typically nonlinear in rotating-polygon systems due to inherent properties of parabolic reflectors, can be constant in a galvanometer-based system (giving a uniform intensity lightsheet) by driving the galvanometer at an unsteady angular velocity. Integrated synchronisation options for the system permit frame-straddling techniques to be used in order to reduce interframe times to below 1/(camera frame rate). The system also offers additional benefits over equivalent double-pulsed or twin-laser setups that rely on beam expansion by lens systems, and that typically only allow measurement at frequencies up to 50 Hz. Manipulation of the beam diameter using lens systems is outlined. The system has been implemented and used to obtain PIV measurements in flows of water and oil.

Keywords: Particle image velocimetry; Scanning laser; Flow visualization; Liquid; Galvanometer

1. Introduction

The recent and rapid improvements in computing power, data transfer and storage, and camera and laser technology, have been hugely beneficial to experimental fluid dynamics. The use of imaging methods allows increasingly detailed spatial and temporal flow features to be studied, without any perturbation of the flow.

Flow properties, whether vectors such as velocity, or scalars such as concentration levels, typically vary temporally and throughout 3-D space. While the development of experimental methods for quantifying fluid flows in 3 dimensions continues [1], it is more common for imaging techniques to measure a 2-D cross-section of a flow, due to ease of implementation.

Usually, the flow of interest is illuminated by using laser light due to its high intensity and low divergence. The illuminated plane is then imaged, and the images are processed to yield a quantitative description of the flow [2].

One such imaging method is Particle Image Velocimetry (PIV), which involves illuminating a flow using a lightsheet, obtaining multiple images of tracer particles embedded in the fluid, and correlating the images to yield mean displacements [3]. Variations in the spatial or temporal lightsheet intensity introduce gradients in the grey level statistics of the images [4]. This can have the undesirable effect of inducing biases in the calculated velocities.

Uniformity of lightsheet intensity is particularly beneficial in the technique of Laser Induced Fluorescence (LIF), where the objective is to quantify a concentration or temperature distribution of a tracer based on image intensity. Correcting images such that their grey levels can be related to the concentration of the tracer involves compensating for a number of artifacts, such as beam attenuation, lens vignetting and non-linearities in the relationship between concentration and fluorescence [5]. Uniform intensity across the length of the lightsheet reduces the complexity of this procedure

* Corresponding author. Tel.: +64 9 3737599; fax: +64 9 3737462.
E-mail address: s.coleman@auckland.ac.nz (S.E. Coleman).

0955-5986/$ - see front matter © 2007 Elsevier Ltd. All rights reserved.
doi:10.1016/j.flowmeasinst.2006.12.003

and facilitates optimisation of experimental parameters in the preparation stage.

Common methods of generating a lightsheet include a continuous-wave (CW) laser combined with a rotating-polygon mirror and a parabolic mirror, and pulsed or CW lasers combined with lens systems. The former approach has limitations of: the polygon mirror (while rotating) not always being positioned at the focus of the parabolic mirror, the mirror combination giving unsteady beam scan velocity across the lightsheet, and a given polygon–parabolic mirror combination only being able to produce a fixed lightsheet width. The first two of these limitations result in nonuniform light intensities across the sheet. Pulsed laser systems rely on beam expansion by lenses (giving a nonuniform Gaussian distribution of light intensity across the sheet) and are limited to generating flow-field image pairs up to the base frequency of the laser unit, typically 50 Hz or less.

In this paper, a cost-effective method of lightsheet generation is presented that is capable of resolving flow fields at frequencies of up to 200 Hz, with recording durations of over 8 min. The method involves a computer-controlled galvanometer mirror positioned at the focus of a parabolic mirror. The galvanometer mirror orientation can be changed in an unsteady fashion such that the laser beam from this mirror, when subsequently reflected by the parabola, scans linearly with time, minimising variations in the intensity distribution of the sheet (lightsheet divergence, and hence intensity variation, being essentially diffraction limited). Additional advantages of the present method of lightsheet generation highlighted below include: the rotating mirror always being positioned at the parabolic-mirror focus, the lightsheet width and beam scan velocity being easily and independently adjustable, and the system facilitating frame-straddling techniques for lightsheet imaging.

2. Fluid flow illumination

Generally the region of the flow field which is of interest is larger than the laser beam diameter, so it is necessary to increase the volume illuminated by the laser in some way. There are two possibilities for doing this: expanding the beam or scanning the beam. Beam expansion results in time-independent illumination, but the lightsheet is spatially varying. Conversely, scanning allows greater control, and thus reduction of the intensity variation, but introduces stroboscopic effects due to the movement of the beam [6].

Expansion of the beam usually involves a cylindrical lens to spread the beam in one direction [3], as shown in Fig. 1. Additional lenses can be used to control the lightsheet thickness, as will be discussed in Section 4. The lightsheet produced by beam expansion with a single lens is diverging, so the energy density decreases with increasing distance from the lens. Since the field of view of the imaging camera is normally rectangular, the divergence results in an intensity variation across the image. Beam expansion is the only option for pulsed lasers due to the short duration of the pulses. The beam can be recollimated using an additional converging lens

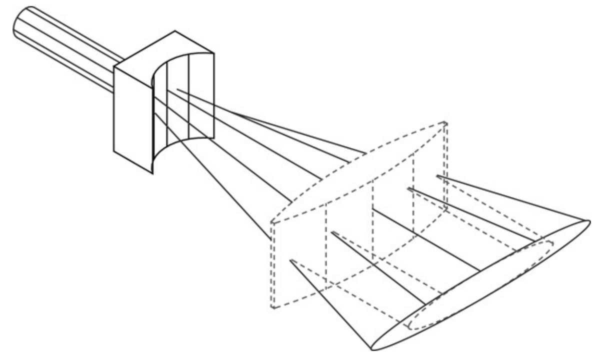

Fig. 1. Diverging lightsheet produced by cylindrical lens.

(dotted lines in Fig. 1), but due to the difficulty and expense in manufacturing lenses of large diameter, this is usually only done for lightsheets whose width does not exceed a few centimeters. Such a lightsheet still has a varying intensity, being brightest in the middle.

A diverging lightsheet can also be produced by reflecting a laser beam off a moving mirror, such as a rotating polygon mirror or a galvanometer-driven mirror. The divergence can be eliminated by using the catacaustic property of parabolas, that rays emanating from the focus of a parabola are reflected such that they become parallel (or conversely, that parallel rays impinging on a parabola converge at the focal point) [7]. This property is unique to parabolas, which accounts for their widespread use as reflectors for satellite dishes and spotlights.

To compare scanning and expanding illumination methods, it is constructive to consider the laser energy reaching a particle within a lightsheet produced by each method. Let the laser power be P, the lightsheet width and thickness be W and Δz respectively, and the particle diameter d_p such that $d_p \ll \Delta z$ (Fig. 2).

For a stationary particle within an expanding lightsheet, the energy received by the particle in a time t_e is approximately $\frac{P t_e d_p^2}{W \Delta z}$. Within a scanning lightsheet of thickness much greater than the particle size, the particle is illuminated by the beam for a time $t_s = \frac{\Delta z}{v_s}$, where v_s is the speed of the lightsheet in the x direction (Fig. 2). During this time, the particle receives $\frac{d_p^2}{\Delta z^2}$ of the energy $P t_s$ available, or $\frac{P d_p^2}{v_s \Delta z}$. If the scanning beam sweeps a distance W in a time t_e ($v_s = \frac{W}{t_e}$), these two energies are the same.

If the particle is moving with velocity v_x in the x direction, it will move a distance $v_x t_e$ while illuminated by the expanded beam, and $\frac{v_x \Delta z}{|v_s - v_x|}$ while lit by the scanning beam. If the scanning velocity is large compared to the flow velocity ($v_s \gg v_x$) and $v_s = \frac{W}{t_e}$, a scanning-beam-illuminated particle image will move a factor $\frac{\Delta z}{W}$ of that obtained when lit by an expanding lightsheet. In capturing the complete lightsheet exposure, particle images will thereby be less blurred for scanning illumination compared to expanding illumination. The difference in the methods is essentially that in the scanning method, the particle receives all its energy in a short time, while in the expanding beam method, the particle receives the same amount of energy in a longer time.

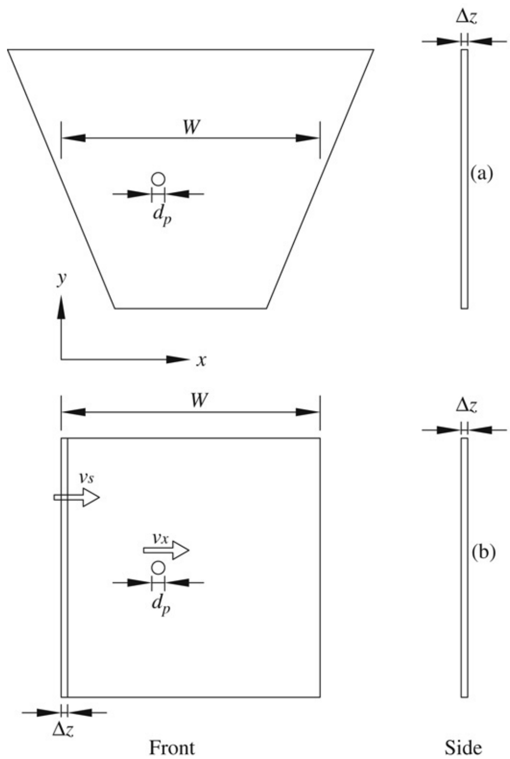

Fig. 2. Lightsheet illumination of particles, (a) Expanding lightsheet, (b) Scanning lightsheet.

If two scanning beam exposures of the flow are taken a time ΔT apart, the time t between successive illuminations of the same particle will be

$$t = \Delta T + \int_{x}^{x+\mathrm{d}x} \frac{1}{v_s} \mathrm{d}x' \tag{1}$$

where x is the particle position in the first image, $\mathrm{d}x$ is the particle displacement between exposures and v_s is the beam scan velocity. To avoid systematic errors, the particle velocity should thus be calculated as

$$v_x = \frac{\mathrm{d}x}{\Delta T + \int_{x}^{x+\mathrm{d}x} \frac{1}{v_s} \mathrm{d}x'} \tag{2}$$

$$v_y = \frac{\mathrm{d}y}{\Delta T + \int_{x}^{x+\mathrm{d}x} \frac{1}{v_s} \mathrm{d}x'}. \tag{3}$$

The integral in Eqs. (2) and (3) can be replaced by $\mathrm{d}x/v_s$ if the scan velocity v_s is uniform, which simplifies and speeds up the image analysis.

With a scanning illumination system, the stroboscopic effect of a moving particle within a moving lightsource must be compensated for unless the scan velocity is sufficiently larger relative to the flow velocity that the integral in Eqs. (2) and (3) can be ignored. This disadvantage is countered by the fact that for a given exposure time, a particle image is less blurred by a scanning beam than an expanded lightsheet.

A related issue which must be considered with scanning beam illumination is the time-lag across the recorded image. In the case of PIV, for example, the vectors obtained from one side of the map will correspond to the velocity at a different time from those at the opposite side, due to the finite time it takes the beam to cross the field of view of the camera. This time discrepancy will affect the calculation of spatial quantities such as vorticity and turbulence statistics. The time lag is equal to the exposure time t_e; in order for the vector map to accurately represent the flow field, the flow field must not change significantly within this time.

But t_e is necessarily less than ΔT, and the method of PIV typically relies on the assumption that the flow velocities are steady between exposures. Hence, if the frame separation ΔT is suitable for PIV, then the effect of scanning is not detrimental to the flow measurements.

The time interval between frames can be written as

$$\Delta T = t_e + t_f + t_a \tag{4}$$

where t_f is the 'flyback' time of the mirror (typically 0.5 ms for the present galvanometer) and t_a is the time during which the mirror is accelerating at the start and end of the scan cycle (0.4 ms). t_e is inversely proportional to the scan velocity, v_s. The minimum value of ΔT corresponds to when $t_e = t_f$; for a typical field-of-view of 10 cm, this represents an upper-limit for the scan velocity of approximately 70 m s^{-1}.

For clear, blur-free particle images, the scan velocity must be significantly greater than the flow velocity, and for this reason, scanning beam illumination is restricted to low-speed flows. The primary research interests at the University of Auckland Hydraulics Group are two-phase flows involving water and sediment, where velocities seldom exceed 1 m s^{-1}. This is considerably less than the scan velocity, so the scanning beam approach (of clearer particle imaging and negligible stroboscopic effects) was therefore deemed suitable for the desired PIV experimental program.

A detailed discussion of the geometry of mirror orientation at a parabolic focus is presented in the following section. This is followed by an examination of the effect of a finite beam diameter in Section 4. The implementation issues for a galvanometer-driven illumination system are then considered in Section 5.

3. Scanning lightsheet geometry

Fig. 3 shows a parabolic mirror whose form is described by the equation

$$y = \frac{x^2}{2L}. \tag{5}$$

The mirror is parabolic in the x direction and planar in the z direction. This discussion considers the optical path within the plane $z = 0$. The focus of the parabolic mirror is located at the point $(0, \frac{L}{2})$. Any wave originating from this focus, restricted to the plane $z = 0$, will be reflected vertically upwards after intercepting the parabola (see Appendix A).

Consider a plane mirror located at the focal point, and a laser beam directed towards this focus at an angle ψ to the y axis. If the angle between the normal to the mirror and the y axis is θ,

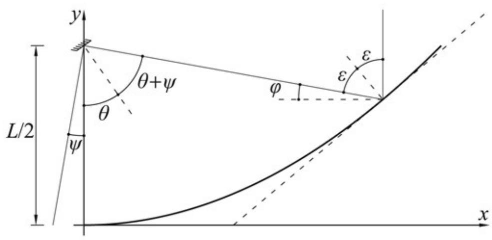

Fig. 3. Mirror arrangement for lightsheet generation.

where $0 \leq \theta \leq \frac{\pi}{2}$, then the laser beam will be reflected along the line

$$y = -\tan(\varphi)\, x + \frac{L}{2} \tag{6}$$

where $\varphi = \frac{\pi}{2} - (2\theta + \psi)$. The intersection of the beam with the parabolic mirror can be determined from Eqs. (5) and (6), rearranging for x, leading to

$$x^2 + 2L\tan(\varphi)x - L^2 = 0. \tag{7}$$

Of the two solutions to Eq. (7), only the positive one is physically plausible, conforming to the law of reflection:

$$x = \frac{-2L\tan(\varphi) + \sqrt{4L^2\tan^2(\varphi) + 4L^2}}{2} \tag{8}$$

$$= L\tan\left(\frac{2\theta + \psi}{2}\right). \tag{9}$$

The lightsheet width can be determined by substituting the maximum and minimum values for the scan angle θ into Eq. (9).

The rate of change of x with respect to θ is

$$\frac{\mathrm{d}x}{\mathrm{d}\theta} = \frac{2L}{1 + \cos(2\theta + \psi)}. \tag{10}$$

The derivative in Eq. (10) increases with increasing angle, θ. Thus, if θ is increasing uniformly, the beam will move along the x axis increasingly quickly. The effect of this is that the pseudo-lightsheet is brighter above the trough of the parabola than at larger values of x.

This is similar to the analysis previously presented by Gray et al. [8] for the case of a rotating polygon mirror. There, the physical size of the polygon was neglected. The effect of the polygon's size is to vary the position at which the beam intercepts the mirror. Rather than originating at a fixed point corresponding to the focal point of the parabola, the beam is reflected from a height which varies by an amount Δr as the polygon rotates:

$$\Delta r = R\left(1 - \cos\frac{\pi}{N}\right) \tag{11}$$

where R is the circumradius and N is the number of faces. Eq. (11) is valid if ψ is small; if this is not the case, then the intersection of the beam and the polygon mirror occurs away from the y axis.

Because the point at which reflection occurs varies as the polygon mirror rotates, rays reflecting off the parabola are no longer parallel (see Appendix A), which increases the divergence in the lightsheet and complicates the intensity variation across it. This distortion is small if the polygon is small in comparison to the parabola ($R \ll L$), but can be eliminated completely by replacing the polygon mirror with a galvanometer mirror.

As Gray et al. [8] pointed out, the variation in lightsheet intensity due to Eq. (10) can be reduced by limiting the range of angles through which the beam is scanned. For regular polygon mirrors, this angle range is determined by the number of faces of the mirror, and equals $\frac{4\pi}{N}$. As ψ and the minimum value of θ are typically small, the width of the lightsheet is primarily dependent on the size of the parabola.

The intensity variation can be eliminated by having the mirror rotate non-uniformly such that the variation in Eq. (10) is compensated for. This is difficult to achieve for a polygon mirror, whose rotational inertia is relatively large, but can be easily done using a galvanometer. An additional advantage of the galvanometer mirror is that the angular range can be readily altered, allowing a variety of lightsheet widths to be produced using the same parabolic mirror.

In order to obtain a lightsheet whose intensity does not vary across its width, the beam must intercept the parabolic mirror at a position x which increases uniformly with time, that is

$$\frac{\mathrm{d}x}{\mathrm{d}t} = v_s \tag{12}$$

where v_s is a constant. Invoking the chain rule and substituting Eq. (10) leads to

$$\frac{\mathrm{d}\theta}{\mathrm{d}t} = \frac{v_s(1 + \cos(2\theta + \psi))}{2L}. \tag{13}$$

Rearranging Eq. (13) and integrating yields

$$\theta = \tan^{-1}\left(\frac{v_s t}{L} + 2c\right) - \frac{\psi}{2} \tag{14}$$

where c is the constant of integration. Setting the boundary condition that $\theta = \theta_0$ at $t = 0$ makes

$$c = \frac{\tan\left(\theta_0 + \frac{\psi}{2}\right)}{2}. \tag{15}$$

A mirror positioned at the focus of a parabola whose angular position is given by Eq. (14) will scan a laser beam at a uniform rate v_s along the x axis. This results in a lightsheet of uniform intensity along the x direction. Furthermore, the stroboscopic correction factors in Eqs. (2) and (3) are simplified by having v_s constant.

4. Beam propagation and lightsheet thickness

In the previous section, non-linear scanning of a laser beam to create a lightsheet of uniform intensity in the x direction was discussed. Here, the intensity distribution across the lightsheet (in the z direction) is considered.

The fundamental mode of a laser beam is described by the Gaussian function, and its width is typically defined in terms

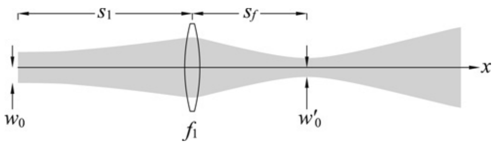

Fig. 4. Beam focussing by a single lens.

of the $\frac{1}{e^2}$ intensity levels [9]. The beam (Fig. 4) has a waist radius w_0 where the beam diameter is a minimum; its radius as a function of x, the distance from the beam waist, is hyperbolic and given by

$$w(x) = w_0 \left(1 + \left(\frac{x}{x_0}\right)^2\right)^{1/2} \tag{16}$$

where x_0 is the *Rayleigh range*, the distance over which the beam increases from w_0 to $\sqrt{2}w_0$. The waist radius is related to the Rayleigh range via

$$w_0 = \left(\frac{\lambda x_0}{\pi}\right)^{1/2} \tag{17}$$

where λ is the beam wavelength and the far-field divergence of the beam θ is given by

$$\theta = \frac{w_0}{x_0} = \frac{\lambda}{\pi w_0}. \tag{18}$$

Thus, the narrower the beam radius, the shorter the Rayleigh range and the larger the beam divergence.

The optimal value of the beam thickness depends on the application. The lightsheet thickness determines the resolution of the plane from which the measurements are obtained, so for planar techniques such as LIF, the thickness should be minimised. Images of thick lightsheets can be considered to correspond to the integral of a number of thin lightsheets, causing 'slab' effects which can affect quantitative results [10]. Such images can also suffer from blurring if the depth of field of the camera lens is small.

If the tracer material used to mark the flow is discrete, as in PIV, rather than continuous, as in LIF, a thin lightsheet can result in signal drop-off as particles move out of the lightsheet due to out-of-plane motion in the flow. The more-stringent rule-of-thumb for autocorrelation analyses is that the out-of-plane motion should be less than $\frac{1}{4}$ of the lightsheet thickness [11]. The optimal lightsheet is therefore thicker for PIV experiments than for LIF experiments [12]. For both techniques, it is desirable for the beam diameter to be approximately uniform throughout the region of interest.

Depending on the application and optical arrangement, the beam diameter may be narrow enough that no optical manipulation is required; if this is not the case, the beam diameter must be reduced using appropriate lenses.

The propagation of a Gaussian beam through an optical system can be calculated using the *ABCD law* [13]. This describes how a complex quantity called the *q-factor* changes as the beam propagates. The q-factor can be defined as

$$q(x) = x + x_{0i} \tag{19}$$

where x is the distance from the beam waist and i denotes the imaginary unit. The q-factor at the output plane, q_o, is related to the q-factor at the input plane, q_i via

$$q_o = \frac{Aq_i + B}{Cq_i + D} \tag{20}$$

where A, B, C and D are the elements of the ray-transfer matrix which describe the optical system between the two planes.

The relevant matrix for transmission over a distance S through a homogeneous medium (such as free-space) is given by

$$M = \begin{vmatrix} 1 & S \\ 0 & 1 \end{vmatrix}. \tag{21}$$

For refraction through a thin lens of focal length f, the appropriate matrix is

$$M = \begin{vmatrix} 1 & 0 \\ -\frac{1}{f} & 1 \end{vmatrix}. \tag{22}$$

The focussing effect of any lens system can be ascertained by using the ABCD law with the appropriate matrix elements. For instance, the effect of a single lens on a Gaussian beam (Fig. 4) can be determined using the matrix representing free-space transmission followed by refraction followed by additional free-space transmission. It is convenient to choose the input plane to be the initial beam waist, since q_i is purely imaginary there [14]. The position (Fig. 4) of the other beam waist, caused by the focussing of the lens, can be located by determining the value of $s_2 = s_f$ which results in the real part of q_o equalling zero. From Eqs. (20)–(22), this occurs at a distance

$$s_f = f_1 + \frac{s_1 - f_1}{\left(\frac{s_1}{f_1} - 1\right)^2 + \left(\frac{x_0}{f_1}\right)^2} \tag{23}$$

from the lens. The Rayleigh range of the focussed beam, x_0', can be obtained from the imaginary part of the q-factor at the focussed beam waist:

$$x_0' = \frac{x_0}{\left(\frac{s_1}{f_1} - 1\right)^2 + \left(\frac{x_0}{f_1}\right)^2}. \tag{24}$$

The focussed beam waist radius, w_0', can be ascertained using Eqs. (24) and (17):

$$w_0' = \frac{w_0}{\sqrt{\left(\frac{s_1}{f_1} - 1\right)^2 + \left(\frac{\pi w_0^2}{f_1 \lambda}\right)^2}}. \tag{25}$$

The beam diameter, $2w(x)$, at any position to the right of the second beam waist at reference distance $x = s_f$ (Fig. 4) can then be determined from:

$$w(x) = w_0' \left(1 + \left(\frac{x - s_f}{x_0'}\right)^2\right)^{1/2}. \tag{26}$$

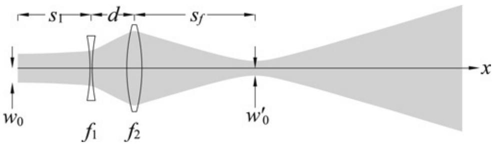

Fig. 5. Beam focussing by a two lens system.

For a two lens system (Fig. 5), the beam profile can be determined using the same method as above, that is by determining the location of the focussed beam waist from the real part of q_o and the Rayleigh range from q_o's imaginary part.

The beam waist for the two lens system is located at

$$s_f = -\frac{f_2(x_0^2 G H_1 + (s_1 H_1 + d f_1)(f_1 H_2 + s_1 G))}{(f_1 H_2 + s_1 G)^2 + x_0^2 G^2} \tag{27}$$

where the parameters $G = d - (f_1 + f_2)$, $H_1 = f_1 - d$ and $H_2 = f_2 - d$ have been introduced as abbreviations. The beam's Rayleigh range is given by

$$x'_o = \frac{f_1^2 f_2^2 x_0}{(f_1 H_2 + s_1 G)^2 + G^2 x_0^2}. \tag{28}$$

The beam diameter after the two-lens system can be determined using Eqs. (27) and (28) in Eqs. (17) and (26). A two-lens system offers greater control of both the location and thickness of the beam waist. For the purposes of lightsheet generation, the focussed beam waist should be located within the region of interest, and the Rayleigh range sufficiently large that the beam diameter does not change significantly throughout the measurement volume.

The finite beam diameter, in addition to determining the lightsheet thickness, results in a focussing effect in the x direction. Because the beam is not a mathematical point, portions of the beam are reflected off points on the galvanometer mirror which are not the focus of the parabola (see Appendix A). Such beams are therefore not vertical after reflection off the parabola (Fig. 6) which results in the focussing and subsequent spreading of the beam. Portions of the beam originating from above the parabolic focus are reflected towards the y-axis, and vice-versa, as demonstrated in Fig. 6 (in which the beam divergence, and hence the focussing effect, has been exaggerated for clarity).

This focussing effect can also be quantified using the ABCD law. The matrix governing reflection from a spherical mirror is given by

$$M = \begin{vmatrix} 1 & 0 \\ \frac{2}{R} & 1 \end{vmatrix} \tag{29}$$

where R is the radius of curvature. R is the reciprocal of the *curvature*, defined as [15]

$$\kappa = \frac{\frac{\mathrm{d}^2 y}{\mathrm{d}x^2}}{\left[1 + \left(\frac{\mathrm{d}y}{\mathrm{d}x}\right)^2\right]^{3/2}}. \tag{30}$$

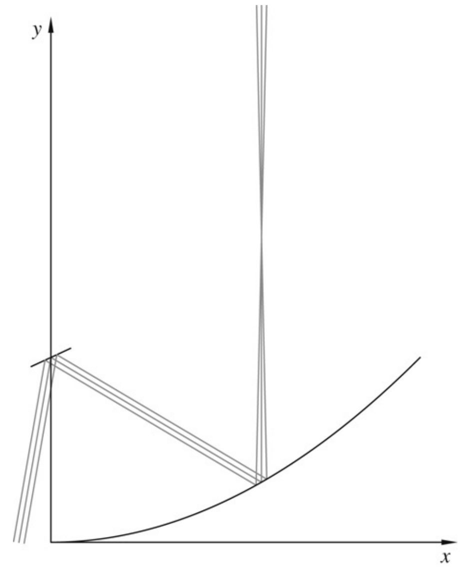

Fig. 6. Focussing effect of parabola on beam of finite thickness.

For a parabola, the radius of curvature is a function of x, given by

$$R(x) = L\left(1 + \frac{x^2}{L^2}\right)^{3/2}. \tag{31}$$

As the beam diameter $2w$ is small relative to L, R can be considered constant (approximating a sphere, and facilitating the use of Eq. (29)) over the area where the beam reflects off the parabola. The radius of curvature is equal to L at $x = 0$, and increases with increasing x.

It is important to note that this focussing occurs in the x direction only; the lightsheet thickness is not affected. The parabolic mirror essentially modifies the beam diameter like a cylindrical lens of focal length $-R(x)/2$. Particles near the focus are illuminated more brightly and for a shorter time than those away from the focus. However, when the beam is moving rapidly relative to the fluid motion, the effect on the particle image is minimal.

5. Implementation

5.1. Lightsheet generation

A scanning beam box (SBB) was assembled to generate the scanning lightsheet described in Section 3. The SBB, shown in Fig. 7, consists of a parabolic mirror ($L = 750$ mm) of horizontal extent 330 mm, and a computer-controlled galvanometer mirror with its reflecting surface positioned at the parabola focus. Two additional beam-steering mirrors are used to direct the beam onto the galvanometer mirror at a small angle to the vertical ($\psi = 5°$).

A frequency-doubled 5W CW Nd:YVO_4 laser (Spectra-Physics Millenia) is used, which has a wavelength of $\lambda = 532$ nm, a $\frac{1}{e^2}$ beam waist of $d_0 = 2.3$ mm, a Rayleigh range of approximately 7 m, and far-field divergence of $\delta \approx 0.3$ mrad. The distance from the laser aperture to the region of interest

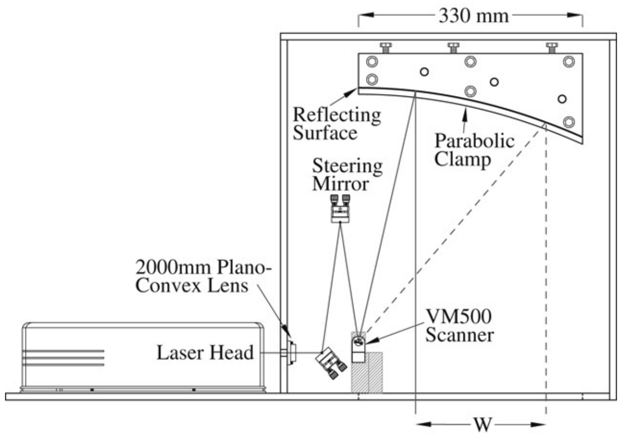

Fig. 7. Scanning beam box.

in the fluid is approximately 2 m, at which point the beam diameter is still less than 2.4 mm. A single, converging lens of focal length 2 m, positioned at the entrance to the SBB, narrows the beam to approximately 0.6 mm at the region of interest.

The parabolic mirror is the only optical component manufactured "in house". A parabolic mount was cut from high-grade aluminium by a computer numerical controlled (CNC) milling machine. A 1 mm thick strip of highly polished stainless steel was clamped to this mount. The stainless steel has a number 8 finish, the most reflective finish commonly produced, corresponding to a surface roughness of approximately $\lambda/4$.

The silver-coated scanning mirror has a 6 mm clear aperture, and is attached to a GSI Lumonics VM500 galvanometer. A Miniature Single Axis (MiniSAX) servo amplifier drives the galvanometer, continuously monitoring and updating the mirror position (within an angle of $\pm 10°$ relative to the reference position) to match the command waveform generated by an SC2000 Digital scanning controller, which connects to a computer via an RS-232 serial interface.

The galvanometer command waveform is computer-created using simple control statements such as "Slew 16383 130", which tells the scanner mirror to move to position 16383 angle units (approximately 10°) over a time period of 130 time units (approximately 3 ms). With a series of commands assembled to generate a complete waveform, this command set is then uploaded to the SC2000 controller, where it continuously loops the commands without further interaction with the computer. Commands can also be used to set sync pins on the SC2000 to high or low at particular positions in the scan cycle, or the galvanometer can be commanded to wait for a change in state of a sync pin before continuing the scan cycle. These sync pin commands are used in the present system to synchronise the scanning mirror to the camera system.

The scanner can be configured to sweep in an unsteady fashion to produce a constant linear velocity laser-beam scan when maximised lightsheet uniformity is required. This is demonstrated in Fig. 8(a), which shows (for a single period of a 200 Hz signal) the active part of the command waveform constructed from 10 linear segments (delimited by crosses)

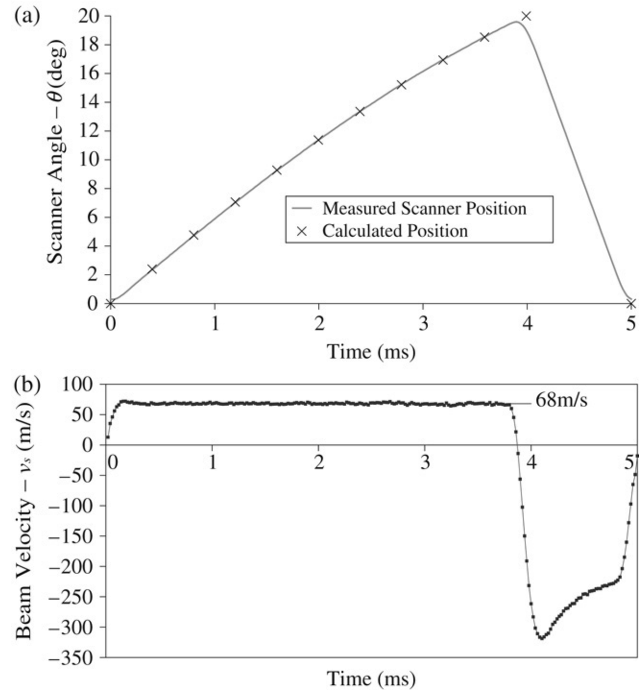

Fig. 8. (a) Graphs of mirror control points (crosses) and measured mirror orientations against time, (b) Graph showing x component of scan velocity against time.

calculated from Eq. (14) (with $\theta_0 = 0$). The final control segment in the diagram returns the mirror to its original orientation so the cycle can repeat. The solid line is the position feedback, which was read from the galvanometer, and which has been adjusted for the galvanometer lag. The velocity at which the beam scans along the x axis was calculated by substituting the measured mirror orientation angle into Eq. (9) as a function of time, and is shown in Fig. 8(b). Except for the first and last 0.2 ms of the scan, where the acceleration of the galvanometer is large, the scan velocity is an approximately constant value of 68 m s^{-1}, indicating that the variation in the lightsheet intensity is minimal, as desired. Triangular-shaped command waveforms (simplified versions of Fig. 8(a) giving a uniform angular mirror velocity) have been found to be adequate for our PIV experiments to date.

5.2. Camera synchronisation

The camera system consists of a Basler A504k camera, a Coreco X64-CL frame grabber, and Streampix image-capture software. The camera is a 1280×1024 pixel, 8 b, monochrome digital camera, with a CMOS sensor capable of capturing a maximum of 500 full resolution images per second. The camera connects to the frame grabber via a CameraLink interface. The frame grabber has 128 MB of on-board frame buffer memory and sits on a 64 b/66 MHz PCI bus that supports data rates of up to 528 MB/s. The Streampix software, developed by Norpix, allows image data to be streamed directly to hard disk drives (6×18 GB 15k RPM SCSI drives attached to an Intel SRCU42X PCI–X raid controller for the present system) in

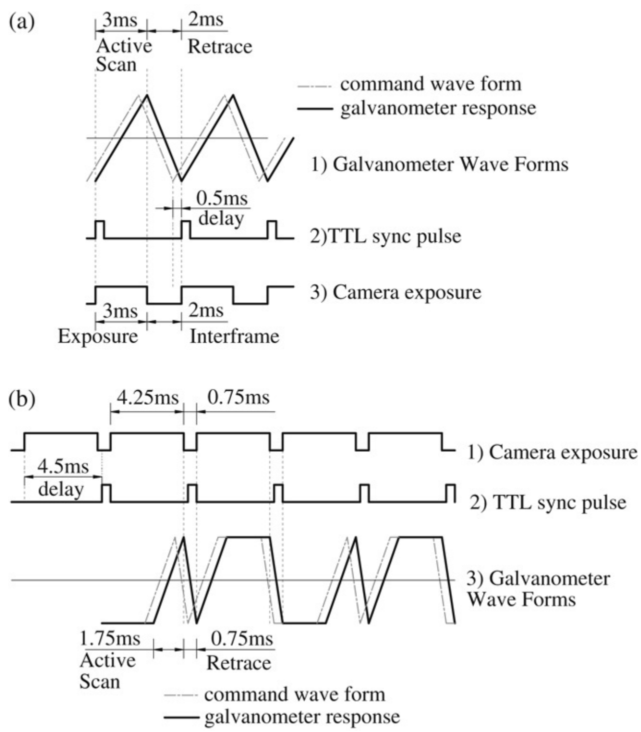

Fig. 9. Galvanometer–camera synchronization: (a) "Galvanometer master", (b) "Camera master".

the host PC. The present drives, configured as a Raid-0 array, support a sustained transfer rate of 200 MB/s across the entire 108 GB of storage space. When operating at a resolution of 960 × 960 pixels and a frame rate of 200 frames per second (fps), there is sufficient storage space to allow for over 8 min of continuous recording.

To capture single-exposure images for cross-correlation, it is necessary to have a single scan of the galvanometer for each camera frame, with the galvanometer retrace positioned between camera exposures. Two synchronisation options are available depending on the time required between successive exposures, which is a function of flow velocity. For interframe times equal to the inverse of camera frame rate, the "galvanometer master" timing shown in Fig. 9(a) is adopted, which allows for interframe times down to 5 ms (for a maximum video streaming rate of 200 fps). For higher flow velocities, the "camera master" timing shown in Fig. 9(b) is adopted, which uses frame straddling to give an effective interframe time of 2.5 ms.

The "galvanometer master" timing uses a sync pulse generated by the scan controller to trigger the camera. As illustrated in Fig. 9(a), the position of the galvanometer mirror lags the command waveform by 0.5 ms due the finite torque of the galvanometer and the rotational inertia of the mirror. To compensate for this lag, the sync pulse is delayed from the start of the command waveform by 0.5 ms using the built in command set for the scan controller. For the present work, a typical example of this timing (which can be varied to suit the measured flow field) is for the camera to run in an external sync mode, capturing a 3 ms exposure (corresponding to the active scan time of the galvanometer) at each sync pulse.

The "camera master" timing uses a sync pulse generated by the frame grabber to trigger the galvanometer. The camera is set in a 200 fps free-run mode with an exposure time of 4.25 ms. The sync pulse is positioned 4.5 ms after the start of a camera frame, or 0.5 ms before the start of the next frame (accounting for the lag of the galvanometer). After receiving the sync pulse, the galvanometer runs a sequence of "idle-active scan-retrace", waits for another sync pulse, and then runs the sequence "active scan-idle-retrace", positioning one active scan at the end of one frame and another at the start of the next. The idle setting corresponds to the galvanometer mirror being parked at either extreme of the scan range where the laser beam is blocked from leaving the SBB. Galvanometer retraces are positioned between camera exposures.

5.3. *Flow-field measurement*

The present Scanning Beam Box (SBB) is currently being used to obtain high-frequency PIV measurements of the motion of both water and oil flows, whose flow velocities are much less than the laser scan velocity.

A sample 200 Hz image and an associated phase-averaged vector map are shown in Fig. 10. The image was captured using an 85 mm Nikon lens with aperture set to f/2.8 and horizontal and vertical field of view equal to 8.5 cm. The exposure time was 3 ms with 10 micron silver coated hollow glass spheres used to seed the flow. These results are from experiments investigating the velocity fields generated by gravity waves above a rippled bed [16]. The wave period was 1 s, and a 50 Hz sequence of vector maps was obtained over a 6 min recording period. Of particular interest for the wave-induced flows were the phase-averages of the vector maps. Due to the finite size of the vector map relative to the wavelength, each column of the vector map corresponded to a slightly different phase. To compensate for this, the phase at each column was calculated independently, by determining the time at which the horizontal velocity was a maximum (this occurring when the wave crest was directly above). The phase-averaging process involved interpolation between vector maps, and also compensated for the small time lag across each vector map due to the finite scan speed of the laser beam.

6. Conclusions

A scanning laser beam PIV system has been designed and implemented that is capable of capturing flow velocity vectors at 200 frames per second (covering typical scales of interest for hydraulic researchers). The scanning lightsheet is generated from a 5W CW 532 nm Nd:YVO_4 laser using a galvanometer-driven mirror together with a parabolic mirror. Image data are captured using a high-speed camera (Basler A504k) and streamed directly to a hard disk array capable of capturing over 8 min of continuous 200 fps high-resolution footage. The system has a number of advantages over rotating-polygon scanning systems, and also over equivalent common double-pulsed and twin-laser systems that rely on beam expansion by

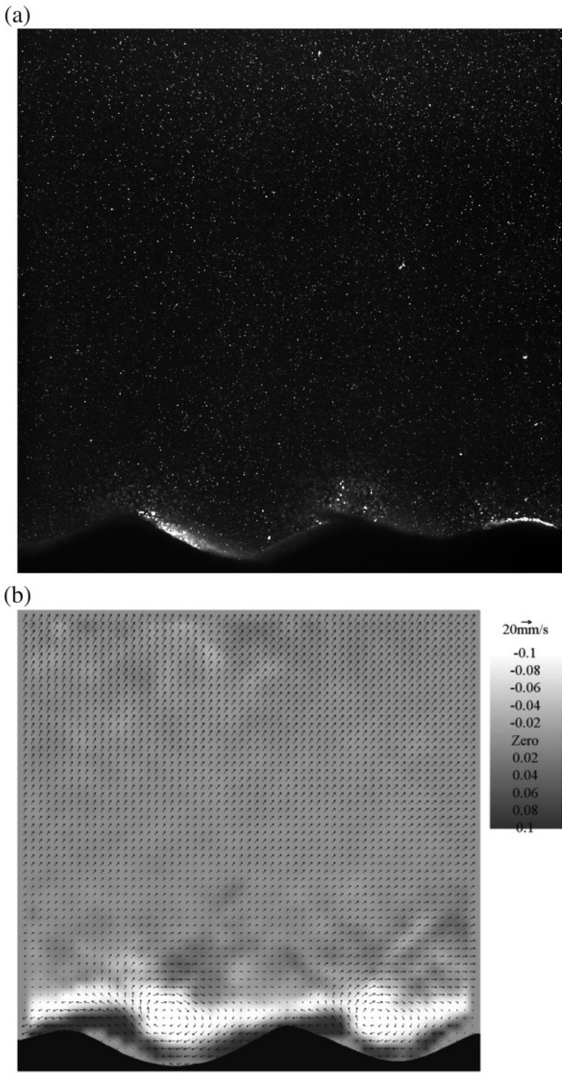

Fig. 10. (a) Image of tracer particles within gravity waves above a rippled bed, (b) Phase-averaged vector map highlighting vortex formation on ripple slopes (velocity vector and vorticity ($\times 10^3\ \mathrm{s}^{-1}$) scalar magnitudes are indicated).

lenses and typically only allow measurement at frequencies up to 50 Hz.

The versatility of the galvanometer system supports a large range of interframe times (down to 2.5 ms) by varying the angular velocity of the scanning mirror. Furthermore, the lightsheet width can be easily varied by altering the angular range of the galvanometer mirror motion – this range of widths being possible for a single size of parabolic mirror, which is not practical with a rotating-polygon mirror system. The galvanometer mirror also always reflects from the focus of the parabola (which is not the case when a polygon mirror is used), minimising any spreading of the beam in the x direction. Manipulation of the beam diameter using lens systems is outlined in the paper.

A uniform intensity lightsheet can be produced with the galvanometer-based system by programming an unsteady scan velocity for the galvanometer mirror (which is not possible for rotating-polygon systems). The subsequent constant linear scan velocity of the laser beam, when reflected from the parabolic mirror, produces a uniform intensity lightsheet that is particularly beneficial for LIF applications, and also facilitates both cross-correlation and auto-correlation approaches for PIV. The constant linear scan velocity of the laser beam also facilitates easy correction of the stroboscopic illumination effect of scanning.

The low mass and moment of inertia of the galvanometer mean that it responds quickly to controlling commands. Combined with trigger support in both the galvanometer and camera systems adopted herein, this allows for simple synchronisation of the two systems, to each other and to external events. Frame straddling is also possible, facilitating interframe times of less than 1/(camera frame rate).

The cost-effective versatile scanning-beam approach described in this paper is limited to CW rather than pulsed lasers. It is ideally suited to experiments involving liquids with flow velocities up to 1 m/s.

Acknowledgements

The authors are appreciative of the comments provided by Simon Miles of Lastek Pty Ltd. (Adelaide, Australia) in regard to concepts and practical details related to the present system.

Appendix A

Here, the reflective properties of a parabola are examined. First, it is shown that all rays coming from the focus of a parabola are parallel after reflection. Then, the direction of a reflected beam originating from an arbitrary point is considered.

A.1. Reflection from focus

A parabola (Fig. 11) can be defined as the set of all points equidistant from a line known as the *directrix* and a point, the *focus* [17]. For the parabola described in this paper, the directrix is $y = -\frac{L}{2}$ and the focus is at $(0, \frac{L}{2})$.

Consider a ray originating from point A, the focus of the parabola, at an angle φ to the horizontal, as shown in Fig. 11. This ray is reflected at point $P(x_p, y_p)$ on the parabola towards A'.

The gradient m_t of the tangent of the parabola (Eq. (5)) is given by

$$m_t = \frac{\mathrm{d}}{\mathrm{d}x}\left(\frac{x^2}{2L}\right) = \frac{x_p}{L}. \tag{32}$$

The gradient of the normal to the tangent, m_n, is therefore

$$m_n = -\frac{L}{x_p} \tag{33}$$

since perpendicular gradients multiply to give -1.

The law of reflection states that the angle of incidence of the ray AP, ϵ, is equal to the angle of reflection. Thus the angle of reflection relative to the horizontal is given by $\varphi + 2\epsilon$.

From Eq. (33), the normal to the tangent at P intersects the y axis at point $B(0, y_p + L)$; the distance AB is therefore $\frac{L}{2} + y_p$.

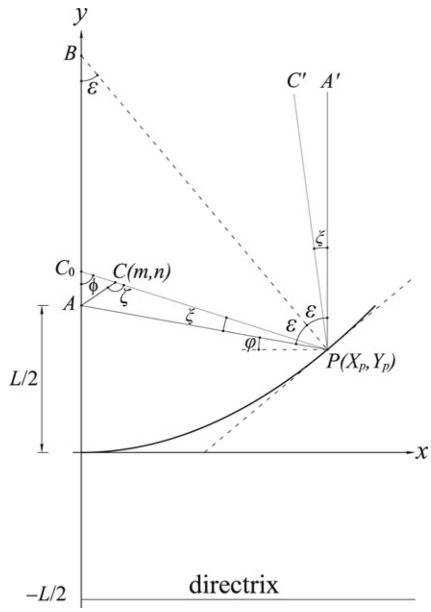

Fig. 11. Geometry of parabola.

But that is also the length of the line AP, from the definition of a parabola, so the triangle *APB* is isosceles. The sum of the internal angles of *APB* is given by

$$\frac{\pi}{2} + \varphi + 2\epsilon = \pi \tag{34}$$

$$\Rightarrow \varphi + 2\epsilon = \frac{\pi}{2}. \tag{35}$$

But $\varphi + 2\epsilon$ is the angle of reflection relative to the horizontal, which shows that each and every reflected ray is vertical, regardless of the angle of incidence.

A.2. Reflection from arbitrary point

Now consider the ray CP (Fig. 11), where C is an arbitrary point in the xy plane, (m, n). Its angle of incidence is $\epsilon - \xi$, so the reflected ray PC' is ξ relative to the vertical.

Applying the sine rule to triangle CAP leads to

$$\sin\xi = \frac{\sqrt{m^2 + (n - \frac{L}{2})^2}}{y_p + \frac{L}{2}} \sin\zeta \tag{36}$$

$$= \frac{c - \frac{L}{2}}{y_p + \frac{L}{2}} \sin\phi \tag{37}$$

where $C_0 = (0, c)$ is the point at which the line CP intersects the y axis:

$$c = n - \tan(\varphi + \xi)m. \tag{38}$$

The angle between the reflected ray PC' and the vertical is therefore

$$\xi = \arcsin\left(\frac{c - \frac{L}{2}}{y_p + \frac{L}{2}} \sin\phi\right). \tag{39}$$

The parameter $c - \frac{L}{2}$ is independent of φ if and only if the point C lies on the y axis. A mirror positioned at $(0, c)$, and rotating such that ϕ changes rapidly with time, will result in a converging lightsheet if $c - \frac{L}{2} > 0$ (corresponding to positive ξ), and a diverging lightsheet if $c - \frac{L}{2} < 0$ (negative ξ). If the mirror is located at the parabola's focus ($c = \frac{L}{2}$), the reflected beam will be vertical regardless of ϕ.

References

[1] Hinsch KD. Three-dimensional particle velocimetry. Meas Sci Technol 1995;6:742–53.

[2] Hesselink L. Digital image processing in flow visualization. Ann Rev Fluid Mech 1988;20:421–85.

[3] Raffel M, Willert C, Kompenhans J. Particle image velocimetry a practical guide. Springer; 1998.

[4] Westerweel J. Digital particle image velocimetry. Delft University Press; 1993.

[5] Ferrier AJ, Funk DR, Roberts PJW. Application of optical techniques to the study of plumes in stratified fluids. Dynam Atmos Oceans 1993;20: 155–83.

[6] Prenel JP, Porcar R, El Rhassouli A. Three-dimensional flow analysis by means of sequential and volumic laser sheet illumination. Exp Fluids 1989;7:133–7.

[7] De Young GW. Exploring reflection: Designing light reflectors for uniform illumination. SIAM Rev 2000;42(4):727–35.

[8] Gray C, Greated CA, McCluskey DR, Easson WJ. An analysis of the scanning beam PIV illumination system. Meas Sci Technol 1991;2: 717–24.

[9] Self SA. Focussing of spherical Gaussian beams. Appl Opt 1983;22(5): 658–61.

[10] Prasad RR, Sreenivasan KR. The measurement and interpretation of fractal dimensions of the scalar interface in turbulent flows. Phys Fluids A 1990;2(5):792–807.

[11] Keane RD, Adrian RJ. Optimization of particle image velocimeters. Part 1: Double pulsed systems. Meas Sci Technol 1990;1:1202–15.

[12] Law AW-K, Wang H, Herlina. Combined particle image velocimetry/planar laser induced fluorescence for integral modeling of buoyant jets. J Eng Mech 2003;129(10):1189–96.

[13] Saleh BEA, Teich MC. Fundamentals of photonics. Wiley-Interscience Publication; 1991.

[14] Kogelnik H, Li T. Laser beams and resonators. Appl Opt 1966;5(10).

[15] Weisstein EW. Curvature. From MathWorld—A wolfram web resource. http://mathworld.wolfram.com/Curvature.html.

[16] Schlicke E, Coleman SE, Nikora VI. A PIV investigation into the interaction between wave motion and sediment ripples. In: 4th IAHR symposium on river coastal and estuarine morphodynamics. 2005. p. 981–9.

[17] Lockwood EH. A book of curves. Cambridge University Press; 1961.